Available online at www.sciencedirect.com

jmr&t Journal of Materials Research and Technology

journal homepage: www.elsevier.com/locate/jmrt

Original Article

# Sonochemical route for mesoporous silica-coated magnetic nanoparticles towards pH-triggered drug delivery system

*Jesús Antonio Fuentes-García* [a,*], *Alex Carvalho Alavarse* [b,c], *Carlos Eduardo de Castro* [b,c], *Fernando Carlos Giacomelli* [b], *Manuel Ricardo Ibarra* [a,d], *Jean-Jacques Bonvent* [b,c], *Gerardo Fabián Goya* [a,d]

[a] *Instituto de Nanociencia y Materiales de Aragón (INMA), Universidad de Zaragoza, 50018, Zaragoza, Spain*
[b] *Centro de Ciências Naturais e Humanas (CCNH), Universidade Federal do ABC, Avenida dos Estados, 5001, Santo André, SP CEP: 09210-580, Brazil*
[c] *NANOMED, Nanomedicine Research Unit, Universidade Federal do ABC, Avenida dos Estados, 5001, Santo André, SP CEP: 09210-580, Brazil*
[d] *Departamento de Física de la Materia Condensada, Facultad de Ciencias, Universidad de Zaragoza, Pedro Cerbuna 12, 50009, Zaragoza, Spain*

ARTICLE INFO

*Article history:*
Received 2 June 2021
Accepted 6 August 2021
Available online 12 August 2021

*Keywords:*
Sonochemistry
Hemocompatibility assay
Magnetic hyperthermia
Release kinetics
Gompertz model

ABSTRACT

This work reports a pH-triggered release system based on core@shell mesoporous magnetic nanoparticles (MNP@mSiO$_2$) obtained using a simple and rapid ultrasound-assisted method. Performed characterization reveals magnetic cores of $Fe_{2.9}Mn_{0.1}O_4$ (38 ± 6 nm) and specific loss power values adequate for hyperthermia (463 W/g), surrounded by a mesoporous silica shell (10 ± 2 nm) with large surface area (269 $m^2\ g^{-1}$) functionalized with hydroxyl groups (-OH). MNP@mSiO$_2$ were loaded with DOX and amino-silane grops, providing pH-triggered DOX release at acidic environments, driving by dipolar intermolecular interactions. The experimental DOX release kinetics at pH 5.5, 6.6 and 7.4 were determined and adjusted to Gompertz dissolution model (Nash–Sutcliffe efficiency coefficient (NSE>0.9)), where the only strongly pH-dependent variable is the percentage of DOX released. The pH-triggered response observed in the system was ~20% of the DOX loaded into the MNP@mSiO$_2$ is released at pH 6.6 or 7.4, whereas up to 80 wt% is released at pH 5.5. Time to 50% of release and dissociation rate of the system remaining constant, suggesting no-pH influence on these parameters. The biological assays highlight negligible hemolytic effect and cytocompatibility of the hybrid material, pointing out the potential use of MNP@mSiO$_2$ as a magnetic driven drug delivery system with pH-triggered drug release kinetics at acidic environments. These results probe the feasibility of sonochemical methods in the elaboration of biocompatible and controlled properties nanomaterials for drug release applications, with the advantage of accurately responses predictions by mathematical model and using minimal processing steps or laboratory equipment.

* Corresponding author.
E-mail address: jesus_spirit69@hotmail.com (J.A. Fuentes-García).
https://doi.org/10.1016/j.jmrt.2021.08.014

## 1. Introduction

The development of colloidal formulations for diagnosis and therapies exploiting the versatility and advantages of nanostructures based on their physicochemical properties may lead to new tailor made nanomedicine options [1]. The landscape of nanomaterials application in nanomedicine is wide, and it covers for instance cardiovascular [2] and ischemic diseases [3], diabetes [4], Alzheimer [5], rheumatoid arthritis [6], glaucoma [7], chronic wounds therapy [8], tissue engineering scaffolds [9] and vascular [10] or tissue regeneration and repair [11]. Concerning particularly to the field of cancer therapies, the drug delivery systems (DDS) can be designed to target specific sites, reducing side effects of currently used chemotherapeutic drugs [12]. The idea behind the DDS is a controlled administration of therapeutic drugs previously loaded to their surface using external stimuli (for instance pH, heat, light) as trigger of the release kinetics [13]. The physicochemical characteristics of a DDS can be rationalized by combining different materials and properties, as well as by controlling their size, shape, surface charge, porosity and biodegradability [14–16]. In this framework, the pH variation represents a stimulus since tumor areas, characterized by a slightly acidic pH (typically ranging from 5.7 to 7.2) due to the high metabolic rates of cancer cells. Moving beyond, if the nanocarriers and captured by the cells through endocytosis, they will experience lower pH ranging from 6.0 to 4.5 in intracellular organelles [17–19]. Accordingly, such knowledge can be exploited to deliver active agents using DDS via a pH-responsive pathway. In addition, the selectivity of DDS between carcinogenic and healthy tissues can be increased, if they are vectorized with active biomolecules for cell targeting [20], it implies physical and chemical modifications. Nevertheless, one outstanding benefit of MNP use is the possibility to drive the colloidal material after their injection to a specific site using the non-ionizing interactions form magnetic field as a remote manipulating tool [21]. Adequate magnetic properties enable the design and elaboration of new formulations created for the treatment of a variety of tumors, aiming reducing side effects, based on easily external spatial manipulation of therapeutic agents and their triggered administration on response to environmental stimulus [22]. Recent strategies for DDS already demonstrated promising results [23] through the combination magnetic cores with amorphous coating for simultaneous magnetically driven vectorization and local-stimulus drug release. In this sense, the potential application of the MNPs reported here for magnetic hyperthermia provides an additional way to construct a synergistic therapeutic at the tumor site [24].

The current tumor cell targeting strategies are based on formulations from different composition and nanoparticle types [25], for instance, mesoporous materials [26], organic-based assemblies [27] and hybrid systems [28]. Mesoporous silica nanoparticles ($mSiO_2$) have been already shown improved DDS administration rates compared to free drugs [29]. Different types of $mSiO_2$ surfaces have been used to increase the volume of drug reservoirs, and specific surface functionalities towards selective loading and triggered release of drugs [30]. The surface chemistry, large surface area, uniform pore size, well-connected pores and biocompatibility are desirable properties of $mSiO_2$ for enhanced loading of cargos, increasing their interest as multifunctional base material for drug delivery, even at clinical trials [31]. Therefore, simpler and faster elaboration methods with minimal infrastructure are required for scaling up the production of these materials to industrial level.

Ultrasound assisted processing for the elaboration of nanomaterials is an interesting tool for the construction of versatile DDS within a reduced time. Sonochemical methods as synthesis routes are efficient tools for the optimization of nanomaterials properties, modifying simple parameters in the experimental conditions for improved physical responses [32–34]. Cavitation produced by ultrasound irradiation in aqueous media generates hot-spots and water hydrolysis reactive radicals that can improve the local conditions for nanomaterials formation and control of their properties faster than colloidal methods [35]. Turbulent agitation within ultrasound-irradiated solutions improves the nanoparticle dispersion, avoiding agglomeration and promoting sonocrystallization [36–38]. This effect exploited for reducing aggregates, provides the conditions for a shell formation on magnetic nanomaterials, characterized for strong interparticle interactions. Besides, intermediate steps such as extraction of surfactants and reactions sub-products removal procedures can be assisted by ultrasound irradiation, avoiding additional separation procedures or thermal treatments, allowing the development of green chemistry based techniques for the elaboration and modification of nanomaterials [39]. These possibilities positioning to ultrasound irradiation-based methodologies as strategies for efficient elaboration and processing of nanomaterials for multifunctional applications.

In this work, a magnetic material with a core–shell structure was developed as a DDS to deliver cytotoxic doxorubicin (DOX) *via* a pH-triggered mechanism. Using a simple sonochemical route, magnetic cores of $Mn_{0.1}Fe_{2.9}O_4$ optimized for heating efficiency were produced with a core–shell structure of mesoporous surface shell (MNP@$mSiO_2$), probing the versatility of proposed sonochemical routes for the core@shell structure elaboration and their potential for DDS applications. The release rate could be accelerated trough acidic environment stimulus, with a release kinetics that is well fitted to a double exponential Gompertz model. The strategy reported here for magnetic-silica core shell structure of the MNPs provides, under adequate manufacture conditions, a specific

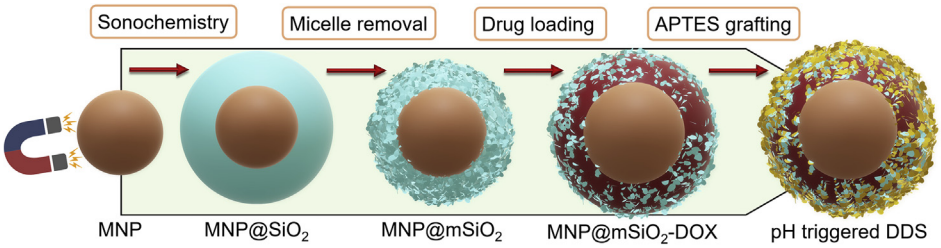


**Fig. 1 – Synthetic strategy towards DDS manufacturing. Using sonochemistry methods, magnetic nanoparticles (MNP) were obtained, then, coated with silica (MNP@$SiO_2$) and cationic micelles. Ultrasound-assisted micelle removal for mesoporous surface (MNP@m$SiO_2$) formation were performed using different solvents for searching enhanced surficial functionality to attaching drugs. Doxorubicin loading (MNP@m$SiO_2$-DOX) and surface functionalization (without ultrasound irradiation) were performed for pH triggered DDS system assembly.**

surface functionality for attaching of DOX due to the use of solvents for micelle removal and the subsequent optimized surface chemistry for DOX loading.

Optimized MNP@m$SiO_2$ surfaces were loaded with DOX trough silane functionalization and the formed amine bonds were used as sensitive entities for pH triggered DOX release. The responses were evaluated under pH 5.5, 6.6 and 7.4 for release kinetics determination and experimental values obtained at different times (1–48 h) were fitted to dissolution-related release Gompertz model, based in a double exponential, one for protonation mechanism and the other for the DOX concentration increase along the experiment time. The comparison between proposed model and experimental values shown proper values of Nash–Sutcliffe efficiency coefficient (NSE) based on root mean square error (RMSE) as normalized goodness-of-fit statistics indicator. The obtained results probes the versatility of sonochemical method for MNP composition manipulation, formation and optimization for drug attaching of mesoporous surface as a tool for DDS elaboration. The evaluation of the obtained pH-sensitive DDS responses were agreed with a dissolution kinetics used for drug dosage forms having good solubility and intermediate release rate. These behavior combined with the shown hemocompatibility and effectivity against cancer cells narrow the gap between the synthetized materials and a secure injectable formulation capable to release drugs according to pH differences in the environment.

## 2. Experimental

The developed synthetic strategy followed in the experimental procedure is schematized in Fig. 1. A chemical route avoiding phase changes was developed exploiting the formation of free radicals, temperature and pressure effects in aqueous solution by ultrasound irradiation. These effects applied to the elaboration of core@shell materials simplifies their synthesis down to two simple steps in the sonochemical process.

The proposed strategy can be consider as the continuation of previous sonochemical studies, where magnetic nanoparticles with homogenous morphology and non-fragmented species were obtained from iron sulfate salt as precursor optimizing their heat efficiency for magnetic hyperthermia applications [40]. While silica encapsulation was adapted from a previous reported on sonochemical route optimization of silica coating thickness based on ultrasound-assisted Stöber aqueous sol–gel method [41]. In this case, the adaptation of these experimental procedure was applied to develop in an easy way a DDS capable to respond to acidic media characteristic of damaged and carcinogenic cells for cancer and anti-tumor therapies applications.

### 2.1. Chemicals

The used chemicals and solvents were all purchased from Sigma–Aldrich. Iron (II) sulfate heptahydrate ($FeSO_4 \cdot 7H_2O$), ACS reagent, ≥99.0%; manganese (II) sulfate monohydrate ($MnSO_4 \cdot H_2O$), ReagentPlus® ≥99%; pellets of sodium hydroxide (NaOH) ACS reagent, ≥97.0%, absolute ethanol ($CH_3CH_2OH$), EMPLURA®; tetraethyl orthosilicate (TEOS, $Si(OC_2H_5)_4$), ≥99.0% GC; cetyltrimethylammonium bromide (CTAB, $CH_3(CH_2)_{15}N(Br)(CH_3)_3$), ≥98%; ammonium hydroxide ($NH_4OH$) solution ACS reagent, 28.0–30.0% $NH_3$ basis; ammonium nitrate ($NH_4NO_3$), ACS reagent, ≥98%; (3-aminopropyl) triethoxysilane (APTES, $H_2N(CH_2)_3Si(OC_2H_5)_3$), 99%; dimethyl sulfoxide (DMSO), ACS reagent ≥99.9%; and Doxorubicin hydrochloride ($C_{27}H_{29}NO_{11} \cdot HCl$), 98.0–102.0% (HPLC). Milli-Q deionized water 18.2 MΩ·cm was used during sample preparation and washing.

### 2.2. MNP sonochemical synthesis

The sonochemical synthesis of MNP used as magnetic core in this research is a modification of previous report on the optimization of parameters for better inductive heating [40]. In this work, the composition of MNP was modified using manganese sulfate salt for manganese ferrite formation during the nucleation and growth, attempting to increase the heating efficiency of MNP as result of elements modification within spinel structures [42]. The irradiation power of ~3.6 W/$cm^2$ was applied using an Ultrasonic Vibra-cell VCX 130 equipment, using the Ti-6A1-4 V 6 mm tip. As reactor, a borosilicate glass bottle ($\varphi = 56$, h = 100 mm) with capacity of 100 mL was employed. A solution (90 mL) containing 262 mg of $MnSO_4$ and 650 mg of $FeSO_4$ in deionized water was prepared.

Stoichiometry was calculated for a $Fe_{2.7}Mn_{0.3}O_4$ ferrite from a 5.4 mM sulfate solution for 20 nm and magnetic hyperthermia optimized MNP (≈300 W/g) as reported in [40]. The prepared solution was sonicated by introducing the tip until 2 cm from the bottom of the flask using nominal values of equipment (130 W, 20 kHz). After 10 min of continuous irradiation, 10 mL of NaOH 2 N solution were poured into the reactor, and the appearance of a dark brown color indicates the formation of MNP. Then, another 10 min for MNP growth in basic media under ultrasonic irradiation were elapsed. Once the irradiation is turned-off, the synthesis solution were dispersed in 90 mL of deionized water, and MNP were precipitated using a magnetic bar. Afterwards, MNP were rinsed with deionized water until pH ≈ 7 in the aqueous dispersion.

### 2.3. Silica coating procedure (MNP@$SiO_2$)

For the silica coating, the following strategy was performed based in the hydrolysis and condensation of TEOS. Starting by suspending the resulting MNP in 90 mL of 60/40 *v/v* absolute ethanol/deionized water and the optimized volume of TEOS for a solid silica coating from previous report in similar reaction conditions [41]. In this work, a mesoporous silica coating was attempted trough organic micelle addition to the reaction. Therefore, continuous ultrasonic irradiation was applied to the solution for 45 min in total. The first 5 min of irradiation allow to improve the MNP dispersion in the ethanol/deionized water solution. Afterwards, 1 mL of TEOS was added to the reactor, followed by 10 min of irradiation for homogenous distribution of silicates and temperature increasing (≈ 60 °C) as result of cavitation effects. Then, 20 mL of $NH_4OH$ mixed with 36.4 mg of CTAB were injected in the reactor for condensation of silicates in presence of surfactant; it allows micelle formation during the shell growth for mesoporous template. The irradiation was turned-off after 30 min, and the obtained solution were diluted using ethanol/water solution to reduce pH and temperature, stopping the silica growth. The obtained nanoparticles were separated by magnetic decantation and washed with absolute ethanol and deionized water, and further centrifuged at 150,000 rpm for 2 min. This procedure was repeated thrice. These samples were labelled as MNP@$SiO_2$, indicating the silica coating, however, at this point the micelle need to be extracted from silica layers for mesoporous surface formation.

### 2.4. CTAB extraction (MNP@m$SiO_2$)

MNP@$SiO_2$ have a residual CTAB template on the silica surface. The heat treatment is a common strategy to remove the quaternary ammonium surfactant (CTAB) from silica-coated surfaces. This process nevertheless generate considerable inter-particle aggregation and may affect their efficacy as DDS [43,44]. On the other hand, treatments using solvents for organic template dissolution have been considered to produce suitable mesoporous surfaces [45,46]. The formation of a satisfactory mesoporous surface indeed depends on the effectiveness over CTAB removal. In the current investigation, the success of this crucial step was evaluated by using three different solvents, and the process was assisted by ultrasonic irradiation for improved dispersion of nanoparticles in the media and better results in the extraction at reduced time. Ethanol-$NH_4NO_3$ (0.075 M), HCl (0.250 M) and ethanol (98%) were employed as solvents [47–50] for extraction efficiency comparison. Ninety-mL of each solvent were used for MNP@$SiO_2$ suspending in the reactor and ultrasonic irradiation during 15 min was applied. Subsequently, the samples were separated by centrifugation and suspended in 10 mL of ethanol, poured in a new fresh solvent, irradiated another 15 min, and finally centrifuged and suspended in 5 mL of ethanol. The samples were further dried in an incubator (60 °C) for 12 h in air atmosphere. The labelling MNP@m$SiO_2$ refers to the nanoparticles with optimized CTAB removal as discussed throughout the manuscript.

### 2.5. DOX loading and surface functionalization (MNP@m$SiO_2$-DOX)

The nanoparticles (30 mg) were added to a 20 mL of DOX aqueous solution at a concentration of 1 mg/mL and kept for 12 h, followed by the addition of 4 μL of APTES. This approach was preferred since APTES functionalization after DOX loading demonstrated better drug confinement by blocking the mesoporous channels [51]. After another 12 h the nanoparticles were centrifuged, washed with deionized water three times and dried in a vacuum chamber for 12 h. The DOX encapsulation efficiency was determined by dissolving 5 mg of the dried sample into 5 mL of DMSO during 4 h. The high solubility of DOX in DMSO ensures quantitative drug extraction. The solution was filtered using an ultrathin membrane (0.45 μm) and diluted for fluorescence spectroscopy measurement (Cary Eclypse, Varian) at $\lambda_{max} = 590$ nm (maximum emission wavelength). The DOX content was determined with the support of a calibration curve (Fig. S1, Supporting Information File) constructed in DMSO. The encapsulation efficiency (EE) was determined as:

$$EE_{\%} = \frac{W_i - W_f}{W_i} \times 100\,\% \quad (1)$$

where $W_i$ is the DOX feeding and $W_f$ is the DOX amount extract using DMSO.

### 2.6. DOX release kinetics

The DOX release from MNP@m$SiO_2$-DOX was investigated at different pH. Fresh PBS solution was prepared in two pH values (7.4 and 6.5) emulates conditions of physiological conditions (i.e blood (7.35–7.45), saliva (6.5–7.2), oral cavity (6.8–7.5)) and acetate buffer solution in pH 5.5 for acidic media environment (i.e. duodenum (5.6–8.0), human skin (5.5), stomach (1–2), cancer cells (6.2–6.9)) for localized therapies. Each solution (5 mL) containing 2 mg of nanoparticles was inserted in a dialysis flask (MWCO 5 kDa) and immersed in deionized water (400 mL) under stirring. At pre-determined times aliquots of 300 μL were sampled and diluted with DMSO for fluorescence spectroscopy measurement and determination of DOX concentration (the dialysis flask was completed with the same amount of fresh sample after each collection). Measurements at each point were performed in triplicate.

The obtained experimental values describing the pH-dependent release kinetics were compared with the three-parameter Gompertz model, derived from the differential equation [52,53]:

$$\frac{dM(t)}{dt} = rM(t)\ln M(t) \tag{2}$$

as generalization of the logistic equation $\frac{dM(t)}{dt} = rM(t)\left[1 - \frac{M(t)}{M_0}\right]$ with the constant growth rate $r$ replaced by a decreasing exponential function (i.e., $r \rightarrow e^{-k(t-T_i)}$), where $a,\ k > 0$ and $T_i$ are the fitting parameters. This model is used mainly for comparing the release profiles of good solubility drugs and intermediate release rate [54], antibacterial activity [55] and release in mesoporous materials [56]. This, in turn, implies that the released concentration is limited by the protonation of functional groups in the system at each pH conditions. Then, the Gompertz model has the solution:

$$M\ (t) = a\ e^{-e^{-k(t-T_i)}} \tag{3}$$

with the parameter $a$ being the mass released as $t \rightarrow \infty$, and $k$ is related to the maximum slope at the inflection point $t = T_i$. One of the advantages of this model is that the obtained values of $a,\ k$ and $T_i$ are easily interpretable in terms of release kinetics. $a$ is the maximum release percentage [%], k is the release rate of drug [$h^{-1}$], and $T_i$ is the time which reflect the time lapse to reach 50% of the total mass released [h].

The goodness-of-fit comparison for the Gompertz model with the release kinetics described by the data obtained from experimental DOX release were developed using the Nash–Sutcliffe Efficiency coefficient (NSE) proposed in [57] a hypothesis testing indicator. Based on the root mean square error $(\mathrm{RMSE}) = \sqrt{\frac{\sum_{i=1}^{N}(O_i - P_i)^2}{N}}$ and standard deviation $(\mathrm{SD}) = \sum_{i=1}^{N}(O_i - \overline{O})^2$ of sample size (N), as follows:

$$NSE = 1 - \left(\frac{RMSE}{SD}\right)^2 \tag{4}$$

where $O_i$ and $P_i$ represent the experimental points in the curve and the Gompertz model forecasting, respectively. This coefficient of efficiency of mathematical predictions has a perfect fit at NSE = 1, and values $-\infty \leq \mathrm{NSE} \leq 1$. In this context, NSE values $\geq 0.9$ can be consider as very good fitting and satisfactory prediction of results [57].

### 2.7. Physicochemical characterization

The detailed structural and morphological characterization of the samples was carried out by transmission electron microscopy (TEM). The TEM images were obtained using a TECNAI F30 field emission gun microscope (FEI Company) operating at accelerating voltage of 300 kV. For sample preparation, a drop of the MNP suspended in water and ethanol for MNP@m$SiO_2$ was deposited on a holey carbon coated micro-grid. TEM images were obtained from dried samples after water evaporation, and the corresponding size histograms were produced and fitted using a Gaussian distribution function $G(d)$ as:

$$G(d) = \sqrt{\frac{2}{\pi}} \times \frac{1}{w} \times exp\left[-2\left(\frac{d-d_0}{w}\right)^2\right] \tag{5}$$

with $w$ and $d_0$ being the full width at half maximum (FWHM) and mean value of the distribution, respectively.

The functional groups of the powdered samples were identified by Fourier transform infrared spectroscopy (FTIR) in attenuated total reflection (ATR) mode using a PerkinElmer 1000 spectrometer. The measurements were carried out from 4000 to 650 $cm^{-1}$. The surface properties of the mesoporous silica shells were probed by $N_2$ surface area analyzer NOVA e-Series (Quantumchrome Instruments). The isotherms were acquired at 77 K and the obtained data were used to calculate the total surface area (BET theory). The pore size distributions were determined by using non-local density functional theory (NLDFT).

### 2.8. Magnetic characterization

Magnetization measurements M(H) at room temperature were performed on dried samples using a commercial SQUID magnetometer (MPMSXL Quantum Design). The powder was conditioned inside plastic capsules as described elsewhere [58]. The magnetization vs. temperature data was obtained in field-cooling and zero-field-cooling modes, using a cooling field $H_{FC} = 100$ Oe.

### 2.9. Heating efficiency measurements

Experiments to measure Specific Loss Power (SLP) under ac magnetic fields were performed in a commercial applicator (DM100 from nB nanoscale Biomagnetics, Spain) with frequencies ranging from 229 to 828 kHz and ac magnetic fields amplitudes $7.95 \leq H_0 \leq 24$ kA/m. The SLP values of the magnetic dispersion containing a total mass of MNP $(m_{NP})$ dispersed in a mass of gelatin $(m_l)$ were calculated as:

$$SLP = \frac{P}{m_{NP}} = \frac{m_l c_l + m_{NP}\, c_{NP}}{m_{NP}} \left(\frac{\Delta T}{\Delta t}\right)_{max} \tag{6}$$

where $c_l$ and $c_{NP}$ are the specific heat capacities of the gelatin and the magnetic nanoparticles, respectively. $\Delta T$ is the temperature variation of the sample measured in a time interval $\Delta t$. Since for the experiments the concentration of MNP is usually in the range of 1% wt., we can approximate $m_l c_l + m_{NP}\, c_{NP} \approx m_l c_l$ and the Eq. (3) can be rewritten as:

$$SLP = \frac{C_l \delta_l}{\varphi}\left(\frac{\Delta T}{\Delta t}\right)_{max} \tag{7}$$

where $C_l$ is the specific heat (4.1 kJ/kg.K) and $\delta_l$ the density (1350 $kg/m^3$) of gelatin, respectively, while $\varphi$ is the mass concentration of the MNP in the sample The heating rate $\Delta T/\Delta t$ in $^{o}C \cdot s^{-1}$ is obtained from the initial temperature increase, within the first 50–100 s of the experiment. $m_{NP}$ was determined as in [40], but in this work, the stoichiometry of ferrite (determined by EDS analysis) in the composition calculation was included.

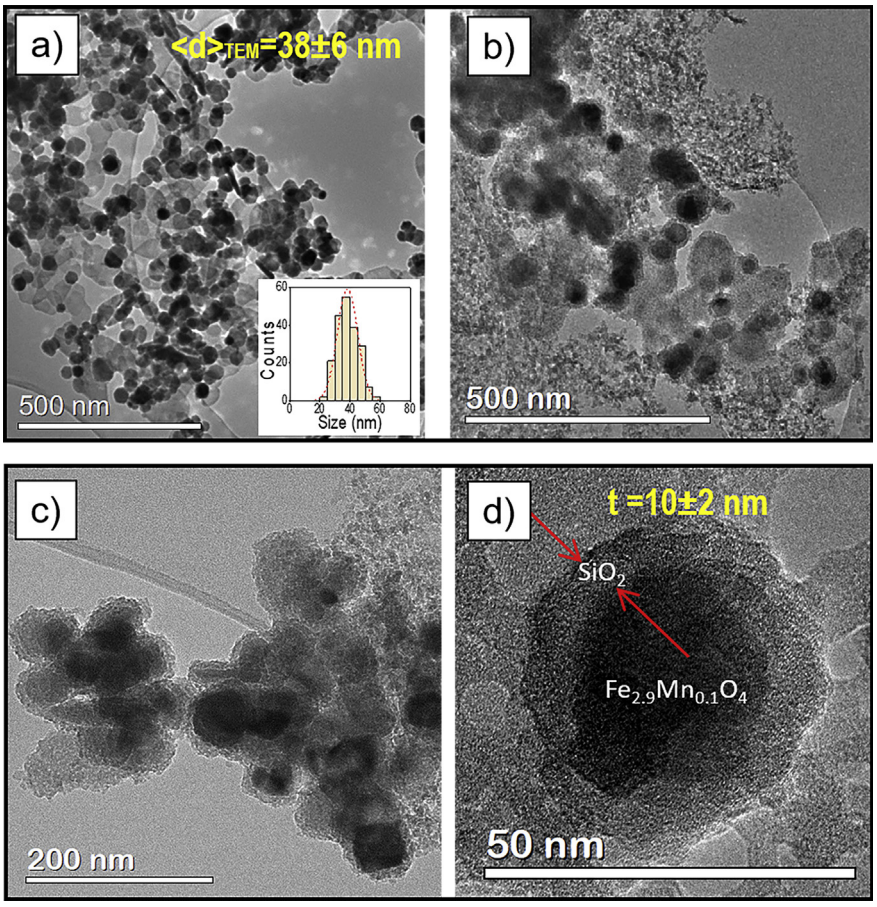


**Fig. 2 – TEM images showing the morphology of the magnetic cores and mesoporous silica-coated (MNP@mSiO$_2$) magnetic nanoparticles: a) as obtained $Fe_{2.9}Mn_{0.1}O_4$ MNP and size distribution histogram (inset) showing an average size 38 ± 6 nm; b) silica-coated magnetic cores, MNP@mSiO$_2$; c) same as b) with magnification to show the structure of MNP@mSiO$_2$ agglomerates; and d) isolated MNP@mSiO$_2$ particle, where the thickness of the silica shell (t = 10 ± 2 nm) is observed.**

### 2.10. *Biological assays*

Hemocompatibility assays were performed (RBCs) according to the ASTM F756 [59]. The blood sample (5 mL) was firstly centrifuged to provide the separation between plasma and RBC, and the cells were then washed with PBS solution (pH 7.4). The RBCs (10 μL solutions in micro centrifuge tubes) were further exposed to nanoparticles (at concentration ranging from 10 to 400 ppm) for 3 h. Afterwards, the cells were lysed by centrifugation and placed in culture plate (98 wells). The absorbance of released hemoglobin from damaged erythrocytes was measured at 580 nm (Synergy HT). Hemolysis percentage was calculated by using the following equation:

$$\text{Hemolysis}_{\%} = \frac{Abs_{NP} - Abs_{nc}}{Abs_{pc} - Abs_{nc}} \times 100 \quad (8)$$

where $Abs_{NP}$, $Abs_{nc}$ and $Abs_{pc}$ are assigned for the absorption of the samples, negative and positive controls. The negative and positive controls were respectively PBS (pH 7.4) and Triton X-100 (2% *v*/*v*) solutions.

As for cell viability investigations, Telomerase immortalized rhesus fibroblasts (Telo-RF) and HeLa cells were cultured in DMEM (Dulbecco's Modified Eagle's Medium) supplemented with 10% FBS, penicillin 10,000 U mL$^{-1}$ and streptomycin 100 mg mL$^{-1}$ at 37 °C in $CO_2$ atmosphere. Initially, 1 × 105 HeLa or Telo-RF cells were seeded into 24-well plates for 24 h. The medium was then replaced by fresh medium and suspensions of nanoparticles (MNP@mSiO$_2$ or MNP@mSiO$_2$-DOX) at final concentration of 100 ppm.

After the incubation time (24h-37 °C), the medium was removed and collected in microtubes, then the cells were washed with 200 μL of PBS and the contents packed in the respective microtube. The same procedure was applied after the cells were harvested by trypsin and later enzymatic inactivation by complete medium. Microtubes were centrifuged (2500 rpm, 6 min), supernatant discarded and the pellets were resuspended in 50 μL binding buffer solution. The cells were labeled with Annexin Alexa 647 (apoptosis) and 7 AAD (necrosis) for 20 min at room temperature protected from light. Then, 150 μL of binding buffer was added and cell viability and mechanism of cell death were probed by flow cytometry (BD FACS CANTO II).

## 3. Results and discussion

After synthesis strategy development and experimental DOX release from MNP@mSiO$_2$, their properties since materials, pH

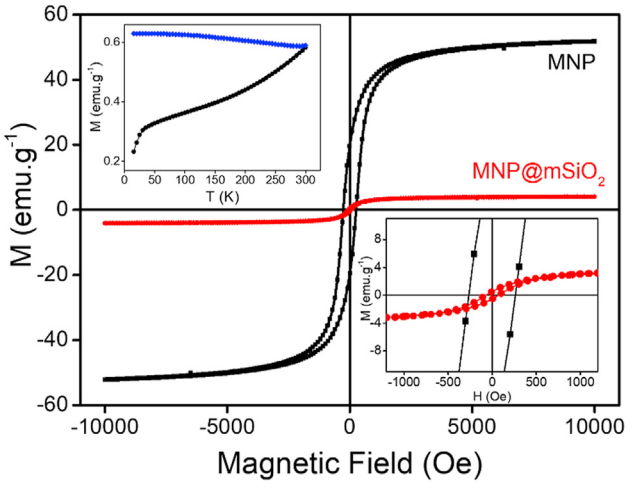


**Fig. 3 – Magnetic data from magnetic cores (MNP) and silica coated (MNP@mSiO$_2$) nanoparticles. Main panel: M vs H hysteresis curves taken at T = 295 K, for magnetic cores (solid squares) and MNP@mSiO$_2$ (solid circles), with an enlarged view of the low-field regions (lower right inset). Zero field cooled and field cooled M vs T data for MNP@mSiO$_2$ particles are shown in the upper left panel.**

dependent response system, safety and effectiveness point of view were evaluated towards pH-triggered DDS.

### 3.1. *Morphological characterization*

The morphological characterization was performed to obtain mainly the size and shape of the synthetized nanomaterials, it allows to evaluate the success of sonochemical method for mesoporous silica core@shell materials. Nearly spherical bare magnetic cores (MNP) were observed from TEM images (Fig. 2a). The size distribution could be fitted using a Gaussian function (inset of Fig. 2a), obtaining an average diameter $\langle d \rangle_{TEM} = 38 \pm 6$ nm. The atomic composition of the MNPs was determined to be $Fe_{2.9}Mn_{0.1}O_4$ from EDX analysis of previously dried samples (Fig. S2, Supporting Information File).

For the samples obtained after the coating process, the TEM image revealed the formation of a core@shell structure (Fig. 2b–c) composed by magnetic cores surrounded by a $SiO_2$ shell of thickness t = 10 ± 2 nm (the red arrows in Fig. 2d). Some agglomeration observed from the TEM images, likely originated by magnetic dipolar inter-particle interactions, besides to the amorphous and rough layer attributed to the mesoporous of the silica coating. Accordingly, the morphological characterization evidences the successful production of single-core and mesoporous magnetic nanostructures by using the ultrasound-assisted synthetic route herein proposed. The single-core configuration achieved in this report is an evidence of the optimized elaboration conditions compared with methodologies that use larger reaction time (>12 h) [60], high-temperature in the synthesis (120 °C) [61], thermal treatments (500 °C) [62], phase changes and organic solvent [63], reducing infrastructure requirements, saving energy and reducing potentially toxic wastes to the environment.

### 3.2. *Magnetic properties*

Magnetic properties modifications are expected on the MNP, before and after their silica encapsulation. The obtained MNP@mSiO$_2$ particles displayed a magnetically soft behavior induced by Mn-contents in the spinel structure [64]. Zero-field cooling (ZFC) and field cooling (FC) data on both bare cores and MNP@mSiO$_2$ showed similar behavior (Fig. 3) of increasing magnetization up to T = 300 K, suggesting that the blocking temperature is above the room temperature. The hysteresis loops at room temperature showed saturation magnetization value $M_S = 52$ emu/g, slightly lower than bulk $MnFe_2O_4$ spinel ferrite [65], whereas MNP@mSiO$_2$ showed more than 10-times lower saturation magnetization ($M_S = 4.1$ emu/g). Estimation of the mass contribution from the diamagnetic $SiO_2$ shell to the total magnetization yielded a ratio of $SiO_2$ and total mass $R = \frac{m_{SiO2}}{m_{total}} = 0.47$ indicating that the drop of magnetization should be around a factor of 2. This difference could be attributed to the $SiO_2$ material in excess attached to the particle clusters as observed in the TEM images. The coercive field $H_C$ of the $MnFe_2O_4$ cores was found to be $H_C = 263$ Oe at room temperature, while $H_C = 66$ Oe for MNP@mSiO$_2$, thus consistent with the blocked state observed from the ZFC-FC data at this temperature. The lower $H_C$ values found in MNP@mSiO$_2$ sample could be due to the presence of the nonmagnetic $mSiO_2$ shell that effectively decreases the magnetic dipolar interactions between magnetic cores.

The heating efficiency of MNP was evaluated by measuring the specific power loss (SLP), which is the power transformed into heat per unit mass under alternating magnetic fields. The measurements were performed in a gelatin matrix to stall the physical rotation of the particles and thus avoid Brownian relaxation contributions, which is the actual condition occurring when in vitro and in vivo experiments are performed. The SLP = 463 W/g value obtained under $H_0 = 24$ kA/m and f = 571 kHz reflects the good heating efficiency of the particles. This value is larger than previously reported data on similar systems (≈ 280 W/g) with very close composition $Fe_{2.03}Mn_{0.97}O_4$ but different synthetic route [66], and than the SLP = 324 W/g under similar measurement conditions in 20 nm size $Fe_3O_4$ MNP.

These results probes the versatility of sonochemical route for easy manipulation of the composition of MNP, while the optimization of the heating performance provides SLP values that could actually allow to combine chemotherapy with local hyperthermia. Additionally, the magnetic cores reported here can be remotely actuated using external magnetic fields, and further optimization of cores is a strategy for achieving multifunctional systems for temperature-triggered DDS from magnetic materials [67].

### 3.3. *Textural properties*

The durg loading capacity of MNP@mSiO$_2$ particles is based on their large surface area given by the mesoporous structure of silica layers, and also relies on the chemistry of available functional groups at the surface. Comparative FTIR spectra after CTAB removal using different solvents (Et (OH), HCl and $NH_4NO_3$) under ultrasonic irradiation as well as control

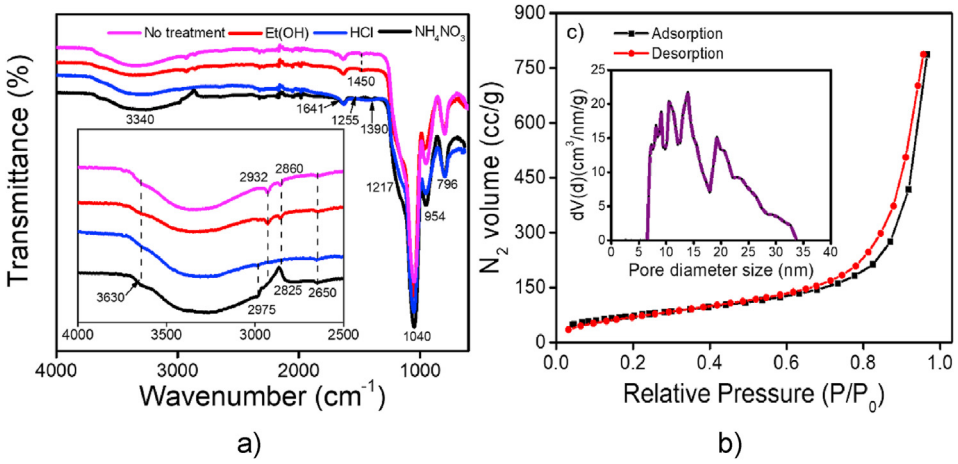


**Fig. 4 – Textural properties of MNP@mSiO$_2$: (a) FTIR spectra of MNP@mSiO$_2$ after CTAB removal using different solvents according to the legend; inset, zoomed FTIR spectra from 4000 to 2500 cm$^{-1}$; (b) BET N$_2$ adsorption/desorption isotherm and inset pore diameter distribution calculated by using the NLDFT method.**

sample (untreated) are given in Fig. 4a. The normal mode at 875 cm$^{-1}$ associated to the tetrahedral site of spinel structure in ferrites [68] was not detected, discarding the presence of bare $Fe_{2.9}Mn_{0.1}O_4$ MNP after silica coating (untreated sample) and CTAB removal using different solvents. Intense frequencies centered at 1217, 1140–1000, 800 and 959 cm$^{-1}$ attributed to Si–O bonding, and persistent bands related to surface hydroxyl groups (3340 and 1641 cm$^{-1}$) of mesoporous silica can be seen in all spectra [69], and the band at 954 cm$^{-1}$ is due to the presence of silanol Si–O stretching, consistent with magnetic core@shell nanoparticles previously reported using sonochemical methods [41].

The assigned signals confirm the formation of silica surface coating the MNP, and any spectral modification of $SiO_2$ matrix was detected after solvent washing. Fig. 4b shows a close-up from 4000 to 2500 cm$^{-1}$ of the FTIR spectra. Within this interval, Et (OH) solution do not show any significant difference compared to the untreated sample, and normal vibrations of the functional groups in CTAB molecule at 2932 and 2860 cm$^{-1}$ attributed to the asymmetrical and symmetrical vibrations of $-CH_2$ bonds, complemented by 1450 cm$^{-1}$ vibration (Fig. 4a) from C–H bending of methyl group in alkane structure confirms the reduced capacity of Et (OH) solution towards CTAB remotion [45]. These vibrations were not detected in the sample labeled as HCl thus implying suitable CTAB extraction. Nevertheless, a persistent signal at 2650 cm$^{-1}$ produced by normal modes of strong carboxylic hydrogen bonding (O–H) was detected in all the samples [70].

The FTIR spectrum of MNP@mSiO$_2$ after $NH_4NO_3$ treatment presents a slight bathochromic shift from 2860 to 2825 cm$^{-1}$ compared to the untreated sample (see Fig. 4a). These effect can be explained by the presence of $NH_4NO_3$ salt in solution as manifested by N–H interactions and confirmed by 1390 and 1525 cm$^{-1}$ vibrations of aliphatic $-NO_2$ radical normal modes [71]. Accordingly, HCl and $NH_4NO_3$ efficiently remove CTAB from mesoporous silica matrix. Yet, a broad band from 3720 to 2860 cm$^{-1}$ suggests more degrees of freedom for –OH and C–H radicals as confirmed by slightly increased vibrations centered at 3630 and 2975 cm$^{-1}$, respectively. The small and broad band centered at 3630 cm$^{-1}$ (3700-3580 cm$^{-1}$) reveals stretching vibrations of O–H bonding in primary (3640 cm$^{-1}$), secondary (3630 cm$^{-1}$) and ternary (3620 cm$^{-1}$) alcohols [72]. These observed signals in the FTIR spectrum of the sample treated with $NH_4NO_3$ suggest more activity of –OH radicals on nanoparticle's surface, bonded to Si–O–Si polymeric chain matrix with Si–OH functional groups available for the attachment of other materials such as drugs, peptides or amino acids [73–75].

The presence of superficial hydroxyl terminations enables for instance DOX adsorption through CO–NH and SiO–NH bonding thanks to the amino groups present at the molecular structure of the chemotherapeutic agent. Therefore, the sample treated with $NH_4NO_3$ was selected for further characterization of nitrogen adsorption/desorption and evaluation as a pH triggered drug delivery system (MNP@mSiO$_2$). The total surface area (269 m$^2$ g$^{-1}$) and total pore volume (1.18 cm$^3$ g$^{-1}$) were determined from BET analysis. The main shape and characteristics of the isotherms (Fig. 4) are similar to those previously reported for mesoporous materials [76], while the hysteretic behavior of the adsorption/desorption process corresponds to the filling/emptying of mesopores by capillary condensation within a non-organized mesoporous structure [77].

The pore diameter distribution curve obtained from non-local density theory (NLDFT) ranges from 5 to 34 nm (Fig. 4c) consistent with a mesopore interval usually considered between 2 nm and 50 nm [78]. The high pore size dispersity can be attributed to agglomeration induced by the magnetic core of the nanoparticles, and the lack of organization of mesoporous matrix on MNP@mSiO$_2$ surface. The pore size distribution is bimodal with a multi-peak broad population at smaller dimensions (6–17 nm) attributed to the mesoporous surface, and another one at higher sizes (from 18 to 34 nm) attributed to inter-particle pore size [79]. The reported results agree with the related literature concerning mesoporous silica nanoparticles evaluated for drug delivery applications [80]. The total surface area, pore volume and silanol coating of MNP@mSiO$_2$ underline the manufactured assembly as a potential candidate for controlled drug delivery.

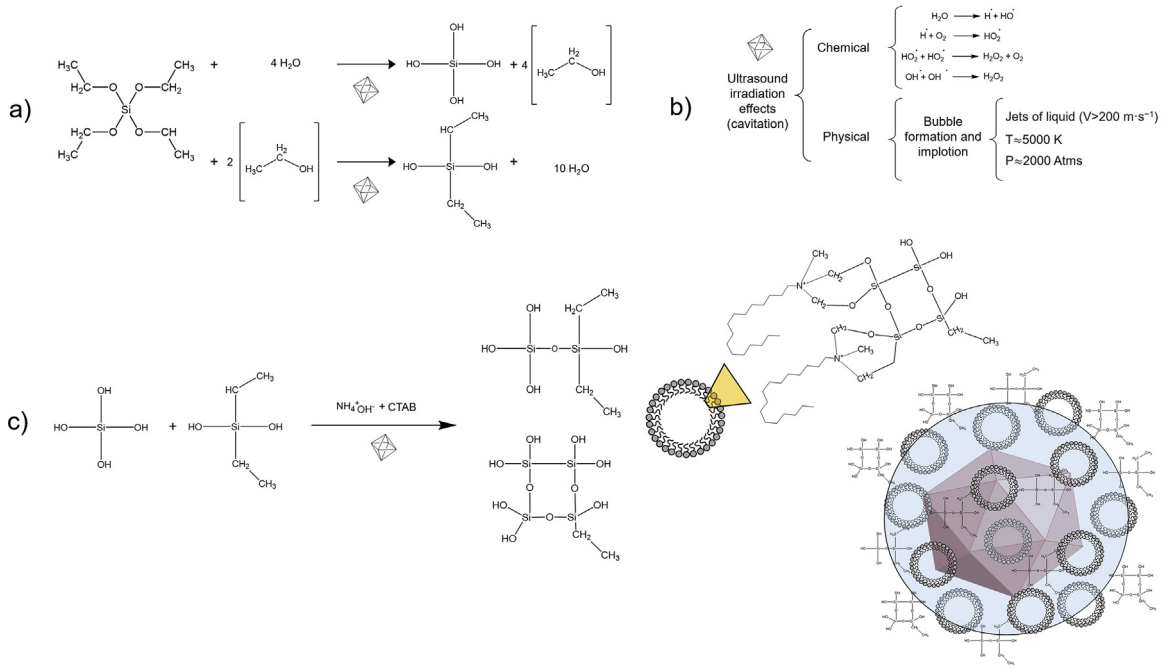


**Fig. 5 – Proposed representation of a mechanism for ultrasound-assisted silica formation. (a) During the hydrolysis of TEOS in the presence of water and ethanol as solvents, silicate based radicals are formed. (b) Ultrasound irradiation effects provides physical and chemical conditions for optimized hydrolysis of TEOS, allowing –OH bonding and high-energetic interchange. (c) Further condensation of silicates in the presence of $NH_4OH$, CTAB and ultrasound irradiation promotes the formation of small micelles and the assembly of silicates trough–OH binding's formation to the surface of micelles and MNP for silica coating.**

Based on the experimental data discussed above, a possible chemical route for the silica encapsulation is proposed, based in the hydrolysis of TEOS (Fig. 5a,b) in the presence of ethanol/water solvent and their condensation (Fig. 5c) using $NH_4OH$ and CTAB.

Both reactions are catalyzed by the ultrasound irradiation effects in aqueous media. Chemical effects of ultrasound irradiation during the reaction include water sonolysis, producing radical formation and high reactivity with –OH functional groups. In addition, physical effects induced by bubble formation and implosion (cavitation) provide unique reaction conditions (pressure, temperature, agitation) that allow to reduce the synthesis time. During the 30 min of condensation, silanol (-SiOH) radicals interact with others (e.g., –OH radicals), forming (Si–O–Si) bonds and interchanging ($–CH_2–CH_3$) radicals to induce the growth of the

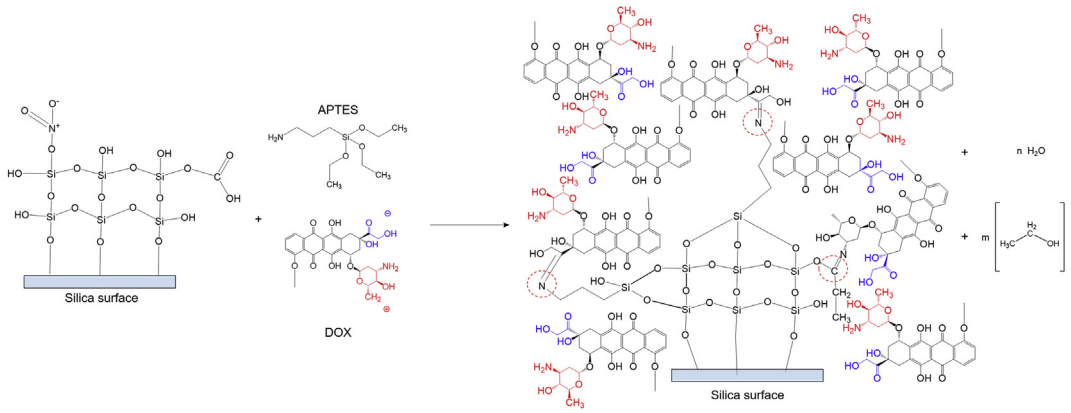


**Fig. 6 – Proposed interactions among functional groups in silica surface, APTES and DOX during the drug loading to MNP@m$SiO_2$ surface. Silicates from APTES graft to silanol (Si–OH) groups in mesoporous surface, while the amine part attach to carboxyl radical of DOX, forming nitrogen-based radicals (dashed red circles) with the capacity of acidic protonation and disengage the anchor for DOX release. Non-attached DOX interacts with other DOX molecules trough intermolecular interactions until equilibria at 12 h of reaction.**

silica layers. In this way, an advantage of the sonochemical protocol used in this work is that it enhances the formation of micelles through the emulsification of the surfactant in aqueous media. We note here that the final pore size dispersion (from BET characterization) could be attributed to agglomeration induced by magnetic interactions of the MNP cores.

After the optimized method for CTAB micelles removal, the produced particles have a silica coating with silanol, amine, carboxyl and ethyl surface radicals. These radicals interacts with silanol groups from APTES hydrolysis in aqueous media (similar to TEOS) and (Si–OH) radicals from mesoporous surface, forming attachments with available amine terminations from APTES molecules (see Fig. 6). The amine radicals from DOX interacts with amine terminations from APTES provides the capacity for pH-controlled response trough Nitrogen-based bonds interchange. If the pH of the surrounding environment of DOX attachment is less than the $pK_a$ (acid dissociation constant (Ka), the logarithmic constant ($pK_a$) is equal to $-\log_{10}(K_a)$) of the functional group, then, the environment can be considered as acidic media and the radical will exist predominately in its protonated form. Besides, when the pH of the environment is higher than the pKa of the functional group, the environment can be considered a basic media and forms radicals in its deprotonated form.

In the equilibria at 12 h of reaction, is important to consider the predominate forms formed by the intermolecular interactions between asymmetric dipoles formed by charge distribution of molecules, DOX molecule have an amine and a carboxyl radical, forming a dipole (Fig. 6) that interacts with other DOX and APTES molecules following electrostatic interactions [81], while another source of intermolecular forces can be the electronegativity of atoms in the functional groups (Si = 1.8; H = 2.1; C = 2.5; N = 3; O = 3.5). An electronegative element is more hydrogen acceptor, forming hydrogen based intermolecular interactions. In this scenario, the pKa plays an importante role to have some idea on the complex process occurring during DOX loading to MNP@$mSiO_2$. In general, amine based functional group protonation occurs at acidic environments, providing the capacity for pH-controlled response trough Nitrogen-based protonation. Then, if the pH of the surrounding environment of DOX attachment is enough to overcome the threshold of pKa of the functional group, the environment can be considered as acidic media and the radical will exist predominately in its protonated form. Besides, when the pH of the environment is higher than the pKa of the functional groups, the environment can be considered a basic media and forms radicals in its deprotonated form. Amine based bonds counts with high-probability in the possible pathway due to the presence of carboxyl and protonated amines from the processing of MMP@$mSiO_2$, as revealed the textural properties.

### 3.4. *DOX release kinetics*

The dependent pH release performance of MNP@$mSiO_2$ was evaluate using as starting value for the experimental DOX's release, the amount of drug loaded in the system. Therefore, encapsulation efficiency of DOX on MNP@$mSiO_2$ was calculated. Based in the resulting EE value (according to Eq. (1)) of 25.1 ± 1.6 wt.% (17.6 μg of DOX per mg of MNP@$mSiO_2$) all experimental values are compared with this concentration to cumulative release percentage determination using the expression

$$\text{Cumulative drug release}\ (\%) = \frac{W_r}{W_m} \times 100\% \tag{9}$$

where $W_r$ is the mass of drug released and $W_m$ is the mass of drug remaining in the system. All curves (see Fig. 7) showed the characteristic S-shaped profile of dissolution-based release responses [82], with an inflexion point and a saturation values occurring (see Table 1 for fitted parameters) after several hours. Many models has been proposed to fit experimental release data for different systems and drugs, and these are often based on sigmoidal functions yielding the expected S-shaped curves for the mass released as a function of time [83].

Usually, a single set of data is fitted using several different models and the final choice is based on the best-fit-criterion (usually the $R^2$ coefficient), without relating the results to any proposed physical model behind the release mechanism [84]. A revision of several sigmoidal functions frequently used for release experiments suggest that the three-parameter Gompertz equation model provided not only the best fit to our data based on the Nash–Sutcliffe model efficiency (NSE) coefficient criterion (see Table 1), but also provides some plausible interpretation of the fitting parameters to understand the pH sensitive release response of MNP@$mSiO_2$-DOX.

From the fitting of the experimental data to the Gompertz model, the total amount of DOX released at pH 7.4 and 6.6 were respectively 21.8 ± 0.7% and 18.4 ± 0.5%, in agreement to the blocking effect expected from the APTES attached to the mesopores that prevents DOX diffusion into the medium. When acetate buffer was used and the pH was lowered to 5.5, the amine functional groups of APTES molecules undergo ionization and diffusion through the aminosilane barrier from the mesopore structure towards the solution. Accordingly, the released DOX amount increased up to 83 ± 2%, a result also

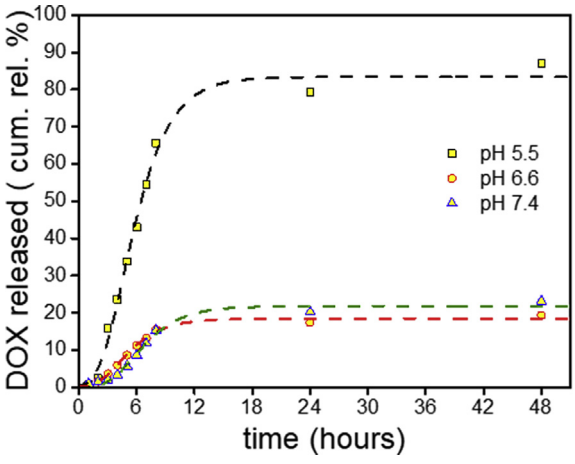


**Fig. 7 – Cumulative DOX release from MNP@$mSiO_2$-DOX in pH 7.4 (blue triangles), 6.6 (red circles) and 5.5 (black squares). The dotted lines are the best fittings obtained by using the three-parameter Gompertz model $M(t) = ae^{-e^{-k(t-T_i)}}$.**

**Table 1 – Parameters obtained for the DOX release kinetics in MNP@mSiO$_2$ at different pH values using Gompertz model. The parameter *a* represents the percentage of maximum release (saturation) of the system, *k* is release rate in [h$^{-1}$], $T_i$ is the time for 50% of total release, RMSE is the root mean square error, standard deviation (SD) from experimental and model data and NSE parameter for goodness-of-fitting.**

| pH | *a* [%] | *k* [h$^{-1}$] | $T_i$ [h] | RSME | $SD_{experimental}$ | $SD_{model}$ | NSE |
|---|---|---|---|---|---|---|---|
| 5.5 | 83.4 | 0.38 | 4.68 | 2.54 | 30.67 | 30.39 | 0.9930 |
| 6.5 | 18.4 | 0.42 | 4.27 | 0.50 | 6.73 | 6.71 | 0.9944 |
| 7.4 | 21.8 | 0.37 | 5.64 | 0.87 | 8.08 | 8.25 | 0.9889 |

previously reported [51]. The parameter *k* obtained from the fits at all pH values was found to be $k = 0.39 \pm 0.07\ h^{-1}$ in all cases, consistent with a single limiting mechanism from the surrounding DOX concentration. This similar *k* values could be associated to the equilibrium dissociation constant ($K_d$) of the complex system formed by APTES-DOX, DOX–DOX, and water-DOX interactions [85], which is weakly dependent on the pH values. Interestingly, the resulting $T_i$ values obtained from the fits were similar varying from $T_i(pH\ 7.4) = 4.2 \pm 0.2\ h$ to $T_i(pH\ 5.5) = 4.7 \pm 0.2\ h$. Therefore, the proposed MNP@mSiO$_2$ nanoparticles are capable to deliver the 50% of the total possible release amount that is pH-dependent in a period within a time window (from 4.2 to 5.6 h) that is independent of pH changes or gradients.

The observed pH-dependent release is consistent with the proposed pathway of DOX loading portrayed in Fig. 6. The DOX release rate is determined by the protonated species that modifies the charge distribution in the molecules present at the nanoparticle's surface. Nevertheless, it is challenging to describe a precise pathway due to the conformational changes in the molecules depending on the dipolar interactions of the attachment. There are many inductive effects in the transmission of charge through the chains formed by APTES and DOX attachment depending on the position of the atoms in the molecule. These inductive effects can be electron-donating to stabilize the positive radicals, or can be electron-withdrawing depending on the electronegativity of the elements (Si = 1.8; H = 2.1; C = 2.5; N = 3; O = 3.5).

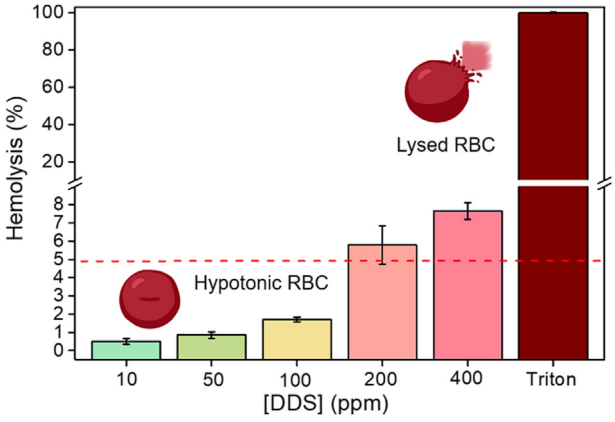


**Fig. 8 – Hemolytic effects of different concentrations of MNP@mSiO$_2$ nanoparticles incubated with red blood cells for 3 h.**

Accordingly, the release behavior at pH 6.6 can be attributed to the carboxyl groups (pKa 3.7–4.8) protonated for unanchor molecules from MNP@mSiO$_2$ surface, thus releasing the DOX molecules. Several (-OH) bonds have the pKa (14–17) to interchange protons and more activity from these radicals is expected at pH 7.4. The experimental data evidence slightly higher DOX release at this condition compared to pH 6.6, thus suggesting more activity of electron interchange due to the (-OH) based bindings formed during DOX loading and exposed at pH 7.4. On the other hand, the amine functional groups (pKa $\approx$ 35) are protonated at pH 5.5 thus notably increasing the amount of released DOX. The exponential behavior evidence at early times (t < 12 h) can be interpreted according to the Gompertz model as the growth rate r representing the DOX release as the result of electron interchange in the molecules, and this is replaced by a decreasing exponential function assigned to the DOX amount in the donor solution.

### 3.5. *Biological assays*

Considering potential intravenous applications of these DDS, we evaluated the in vitro hemolytic effects by exposing RBC to the manufactured nanoparticles according to established protocols. The experimental results are given in Fig. 8. Based on the ISO 10993-1:2009, negligible damage to red blood cells has been evidenced up to the concentration of 100 ppm. According to this standard, hemolytic materials are those with hemolytic indexes higher than 5%. The hemolytic behavior is nevertheless dose-dependent and the produced nanomaterial starts to be hemolytic at the concentration of 200 ppm. Possibly, at relatively high concentrations, the deposition of aggregates at the surface of RBC may cause membrane damage and further release of cytoplasmic hemoglobin. Additionally, the nanoparticles were able to cover considerable fractions of the cell surface, thereby reducing the nutritional supply, and leading to a deficiency of metabolic energy (ATP). These unexpected changes can cause membrane rupture at lower than expected osmotic pressures [86].

The cell viability has been further evaluated by flow cytometry analysis, and the experimental data are reported in Fig. 7. The cell viability assays were performed at the concentration of 100 ppm taking into account the previously reported hemolytic effects. In such a condition, the results evidence the biocompatibility of the produce nanoparticles as drug-free agents, regardless the cell line. This conclusion is based on the ISO 10993-5:2009 which considers cytotoxic materials those where the cell viability is reduced by more than 30% compared to the control (untreated cells).

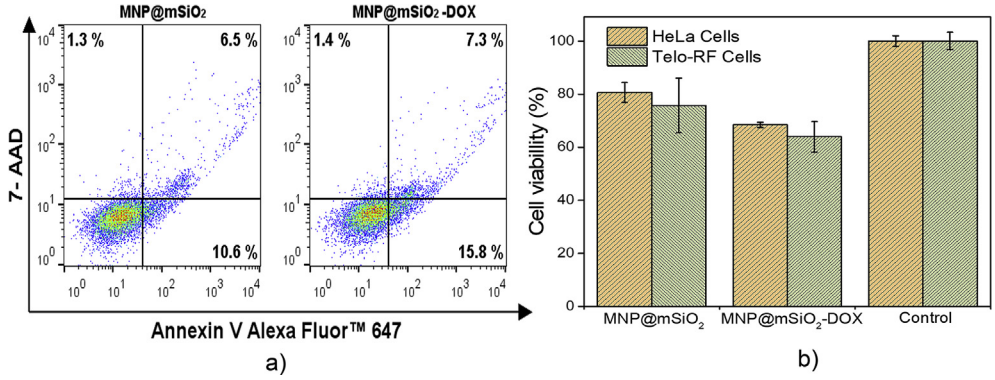


**Fig. 9 – Biological evaluation. (a) Two-dimensional dot-plots for the determination of live, apoptotic and necrotic HeLa cells exposed to the same nanoparticles. (b) Viability of Telo-RF and HeLa cells in contact with MNP@mSiO$_2$ and MNP@mSiO$_2$-DOX at 100 ppm for 24 h.**

The DOX molecule is known to trigger apoptotic processes [87], consistent with the flow cytometry data for HeLa cells. In Fig. 9, both viable and necrotic (7-AAD positive staining) cells appear respectively in the lower left and upper left quadrants, whereas apoptotic cells (Annexin V Alexa Fluor™ 647 positive/7-AAD negative) appear in the right quadrants. Accordingly, the reported data evidence high cell viability (the majority of the dots appear in the lower left quadrant). Furthermore, the cell death is primarily associated to early apoptosis (lower right quadrant). Indeed, apoptosis is a programmed cell death much less traumatic than necrosis. The apoptosis is a process that generally occurs without inflammation or injury to surrounding tissues since the cell membrane usually remains intact until be cleared by phagocytes. On the other and, due to the loss of membrane integrity, necrotic cells release intracellular contents to the surroundings, potentially inducing inflammations.

The cytoprotective nature of the silica coating is therefore evident thanks to its high biocompatibility [88] which is commonly attributed to the presence of the silanol groups and surface –OH radicals which avoid cell damage triggered by charge affinity. Indeed, iron-based metallic MNP are typically cationic systems, therefore with high affinity to electronegative components of the cell membrane, which potentialize cell damage and ultimately, cell death [89]. The silica coating thus provides chemical stability and biocompatibility to the prepared material. The DOX-containing assemblies, on the other hand, are already cytotoxic (cell viability < 70%). This is possibly caused by the DOX release at the pH of the cell medium (~20% of DOX is released after 24 h at pH 7.4 as evidenced in Fig. 5). The behavior is essentially independent on the cell line since the data reported for HeLa and Telo-RF are not statistically different if one takes into account the reported error bars.

The percentage of early apoptotic cells increases for MNP@mSiO$_2$ -DOX compared to MNP@mSiO$_2$, thus confirming DOX damage via an apoptotic process. This damage is supposed to the boosted at slightly acid pH where DOX release is enhanced as evidenced in Fig. 5. Accordingly, the DOX-loaded manufactured nanoparticles may constitute a step forward with regard to the use of stimuli-sensitive assemblies to respond the well-known tumor acidosis. The hybrid material can be potentially driven through a site of action by using a magnetic field, the pH-responsive behavior is expected to conduct cargo release preferentially in localized acidic media (such as in tumor tissues), and DOX-induced apoptotic cell death is indeed preferred to avoid unwanted side effects in surrounding healthy tissues. Additionally, the process can be conducted by exposing tumor sites to temperatures higher than the normal body temperature via magnetic hyperthermia, thus aiding damaged cell death by apoptosis.

## 4. Conclusions

The reported ultrasound-assisted strategy for the synthesis and processing of MNP@mSiO$_2$ represent a simple and scalable option for the elaboration of single-core magnetic nanomaterials with potential use in the biomedical field. The synthesis route presented here allows to modify the materials characteristics and properties (mesoporous structure, magnetic response) substituting of adding reactants in a controlled way. The reaction mechanism, which is catalyzed by the ultrasonic irradiation in aqueous solution (i.e., cavitation, radicals formation) is the basis for the reduced time to produce properly functionalized DDS.

The proof of concept using DOX loaded at MNP@mSiO$_2$ surface showed good release times and pH-sensitive kinetics, that could be interpreted by the three free parameters of the Gompertz model (NSE>0.9). The kinetics is consistent with the unblocking effect of the APTES attached to the mesopores, releasing DOX into the medium at acidic pH. The pH-dependent parameter of the model ($a$), reflects the maximum percentage of released DOX while $k$ and $T_i$ are characteristic of the specific release mechanism of the system, remaining constant in all cases. These response combined with its applicability for anti-cancer drug delivery therapies based in amine attaching close the gap between anti-cancer easily elaborated nanostructured DDS and personalized applications of nanomaterials in this field. This methodology could be extended to other proof-of-concept cytotoxic drugs with amine functional

groups in their structures, which could constitute a new class of injectable pH-sensitive systems for targeted drug release. Last but not least, these materials can be elaborated at reduced processing costs and time, on the way to green industrial manufacturing, saving energy and reducing toxic waste to environment derived of synthesis procedures.

## Funding

This work was partially supported by the Spanish Ministerio de Ciencia, Innovación y Universidades (project PID2019-106947RB-C21), FAPESP, Brazil (Grant 2014/50983-3) and CAPES, Brazil (Grant 88881.189090/2018-01). FCG acknowledges the financial support provided by FAPESP (Grant 2019/06634-8).

## Availability of data and material

Data is contained within the article or Supplementary Materials.

## Declaration of Competing Interest

The authors declare that they have no known competing financial interests or personal relationships that could have appeared to influence the work reported in this paper.

## Acknowledgments

ACA, CEC and JJB are grateful to CEM-UFABC for allowing access to its facilities. JAF, MRI and GFG would like to acknowledge the use of Servicio General de Apoyo a la Investigación-SAI, Universidad de Zaragoza.

## Appendix A. Supplementary data

Supplementary data to this article can be found online at https://doi.org/10.1016/j.jmrt.2021.08.014.

## REFERENCES

[1] Germain M, Caputo F, Metcalfe S, Tosi G, Spring K, Åslund AKO, et al. Delivering the power of nanomedicine to patients today. J Control Release 2020;326:164–71. https://doi.org/10.1016/j.jconrel.2020.07.007.

[2] Salehi B, Del Prado-Audelo ML, Cortés H, Leyva-Gómez G, Stojanović-Radić Z, Singh YD, et al. Therapeutic applications of curcumin nanomedicine formulations in cardiovascular diseases. J Clin Med 2020;9:746. https://doi.org/10.3390/jcm9030746.

[3] Hu B, Boakye-Yiadom KO, Yu W, Yuan ZW, Ho W, Xu X, et al. Nanomedicine approaches for advanced diagnosis and treatment of atherosclerosis and related ischemic diseases. Adv Healthc Mater 2020;9(16):2000336. https://doi.org/10.1002/adhm.202000336.

[4] Lemmerman LR, Das D, Higuita-Castro N, Mirmira RG, Gallego-Perez D. Nanomedicine-based strategies for diabetes: diagnostics, monitoring, and treatment. Trends Endocrinol Metab 2020;31:448–58. https://doi.org/10.1016/j.tem.2020.02.001.

[5] Wilson B, Geetha KM. Neurotherapeutic applications of nanomedicine for treating Alzheimer's disease. J Control Release 2020;325:25–37. https://doi.org/10.1016/j.jconrel.2020.05.044.

[6] Jeong M, Park J-H. Nanomedicine for the treatment of rheumatoid arthritis. Mol Pharm 2020;18(2):539–49. https://doi.org/10.1021/acs.molpharmaceut.0c00295.

[7] Kwon S, Kim SH, Khang D, Lee JY. Potential therapeutic usage of nanomedicine for glaucoma treatment. Int J Nanomed 2020;2020:15:5745–65. https://doi.org/10.2147/IJN.S254792.

[8] Sharifi S, Hajipour MJ, Gould L, Mahmoudi M. Nanomedicine in healing chronic wounds: opportunities and challenges. Mol Pharm 2020;18(2):550–75. https://doi.org/10.1021/acs.molpharmaceut.0c00346.

[9] Malek-Khatabi A, Javar HA, Dashtimoghadam E, Ansari S, Hasani-Sadrabadi MM, Moshaverinia A. In situ bone tissue engineering using gene delivery nanocomplexes. Acta Biomater 2020;108:326–36. https://doi.org/10.1016/j.actbio.2020.03.008.

[10] Cui W, Wang A, Zhao C, Zhu W. Editorial: nanotechnology in cardiovascular regenerative medicine. Front Bioeng Biotechnol 2020;8:608844. https://doi.org/10.3389/fbioe.2020.608844.

[11] Cui L, Liang J, Liu H, Zhang K, Li J. Nanomaterials for angiogenesis in skin tissue engineering. Tissue Eng-Part B Rev 2020;26:203–16. https://doi.org/10.1089/ten.teb.2019.0337.

[12] Li W, Peng A, Wu H, Quan Y, Li Y, Lu L, et al. Anti-cancer nanomedicines: a revolution of tumor immunotherapy. Front Immunol 2020;11:3346. https://doi.org/10.3389/fimmu.2020.601497.

[13] Moradi Kashkooli F, Soltani M, Souri M. Controlled anti-cancer drug release through advanced nano-drug delivery systems: static and dynamic targeting strategies. J Control Release 2020;327:316–49. https://doi.org/10.1016/j.jconrel.2020.08.012.

[14] He C, Hu Y, Yin L, Tang C, Yin C. Effects of particle size and surface charge on cellular uptake and biodistribution of polymeric nanoparticles. Biomaterials 2010;31:3657–66. https://doi.org/10.1016/j.biomaterials.2010.01.065.

[15] Dreaden EC, Austin LA, MacKey MA, El-Sayed MA. Size matters: gold nanoparticles in targeted cancer drug delivery. Ther Deliv 2012;3:457–78. https://doi.org/10.4155/tde.12.21.

[16] Truong NP, Whittaker MR, Mak CW, Davis TP. The importance of nanoparticle shape in cancer drug delivery. Expert Opin Drug Deliv 2015;12(1):129–42. https://doi.org/10.1517/17425247.2014.950564.

[17] Boedtkjer E, Pedersen SF. The acidic tumor microenvironment as a driver of cancer. Annu Rev Physiol 2020;82:103–26. https://doi.org/10.1146/annurev-physiol-021119-034627.

[18] Liu J, Huang Y, Kumar A, Tan A, Jin S, Mozhi A, et al. PH-Sensitive nano-systems for drug delivery in cancer therapy. Biotechnol Adv 2014;32:693–710. https://doi.org/10.1016/j.biotechadv.2013.11.009.

[19] He X, Li J, An S, Jiang C. PH-Sensitive drug-Delivery systems for tumor targeting. Ther Deliv 2013;4:1499–510. https://doi.org/10.4155/tde.13.120.

[20] Mout R, Moyano DF, Rana S, Rotello VM. Surface functionalization of nanoparticles for nanomedicine. Chem Soc Rev 2012;41:2539–44. https://doi.org/10.1039/c2cs15294k.

[21] Xia Y, Sun J, Zhao L, Zhang F, Liang X-J, Guo Y, et al. Magnetic field and nano-scaffolds with stem cells to enhance bone regeneration. Biomaterials 2018;183:151–70. https://doi.org/10.1016/J.BIOMATERIALS.2018.08.040.
[22] Hervault A, Dunn AE, Lim M, Boyer C, Mott D, Maenosono S, et al. Doxorubicin loaded dual pH- and thermo-responsive magnetic nanocarrier for combined magnetic hyperthermia and targeted controlled drug delivery applications. Nanoscale 2016;8:12152–61. https://doi.org/10.1039/c5nr07773g.
[23] Hervault A, Thanh NTK. Magnetic nanoparticle-based therapeutic agents for thermo-chemotherapy treatment of cancer. Nanoscale 2014;6:11553–73. https://doi.org/10.1039/c4nr03482a.
[24] Harmon BV, Takano YS, Winterford CM, Gobé GC. The role of apoptosis in the response of cells and tumours to mild hyperthermia. Int J Radiat Biol 1991;59:489–501. https://doi.org/10.1080/09553009114550441.
[25] Kim CS, Tonga GY, Solfiell D, Rotello VM. Inorganic nanosystems for therapeutic delivery: status and prospects. Adv Drug Deliv Rev 2013;65:93–9. https://doi.org/10.1016/j.addr.2012.08.011.
[26] Kesse S, Boakye-Yiadom K, Ochete B, Opoku-Damoah Y, Akhtar F, Filli M, et al. Mesoporous silica nanomaterials: versatile nanocarriers for cancer theranostics and drug and gene delivery. Pharmaceutics 2019;11:77. https://doi.org/10.3390/pharmaceutics11020077.
[27] Jäger E, Giacomelli F. Soft matter assemblies as nanomedicine platforms for cancer chemotherapy: a journey from market products towards novel approaches. Curr Top Med Chem 2015;15:328–44. https://doi.org/10.2174/1568026615666150130152300.
[28] Karimi M. Advances in nanomaterials for drug delivery: polymeric, nanocarbon and bio-inspired. IOP Publishing; 2018. https://doi.org/10.1088/2053-2571/aadd7c.
[29] Gao Y, Gao D, Shen J, Wang Q. A review of mesoporous silica nanoparticle delivery systems in chemo-based combination cancer therapies. Front Chem 2020;8:598722. https://doi.org/10.3389/fchem.2020.598722.
[30] Rea I, Terracciano M, De Stefano L. Synthetic vs natural: diatoms bioderived porous materials for the next generation of healthcare nanodevices. Adv Healthc Mater 2017;6:1601125. https://doi.org/10.1002/adhm.201601125.
[31] Bobo D, Robinson KJ, Islam J, Thurecht KJ, Corrie SR. Nanoparticle-based medicines: a review of FDA-approved materials and clinical trials to date. Pharm Res 2016;33:2373–87. https://doi.org/10.1007/s11095-016-1958-5.
[32] Wang Y, Nkurikiyimfura I, Pan Z. Sonochemical synthesis of magnetic nanoparticles. Chem Eng Commun 2015;202:616–21. https://doi.org/10.1080/00986445.2013.858039.
[33] Bang JH, Suslick KS. Applications of ultrasound to the synthesis of nanostructured materials. Adv Mater 2010;22:1039–59. https://doi.org/10.1002/adma.200904093.
[34] Barcikowski S, Plech A, Suslick KS, Vogel A. Materials synthesis in a bubble. MRS Bull 2019;44:382–91. https://doi.org/10.1557/mrs.2019.107.
[35] Fuentes-García JA, Santoyo-Salzar J, Rangel-Cortes E, Goya GF, Cardozo-Mata V, Pescador-Rojas JA. Effect of ultrasonic irradiation power on sonochemical synthesis of gold nanoparticles. Ultrason Sonochem 2021;70:105274. https://doi.org/10.1016/j.ultsonch.2020.105274.
[36] Ruecroft G, Hipkiss D, Ly T, Maxted N, Cains PW. Sonocrystallization: the use of ultrasound for improved industrial crystallization. Org Process Res Dev 2005;9:923–32. https://doi.org/10.1021/op050109x.
[37] Luque de Castro MD, Priego-Capote F. Ultrasound-assisted crystallization (sonocrystallization). Ultrason Sonochem 2007;14:717–24. https://doi.org/10.1016/j.ultsonch.2006.12.004.
[38] Kim HN, Suslick KS. The effects of ultrasound on crystals: sonocrystallization and sonofragmentation. Crystals 2018;8. https://doi.org/10.3390/cryst8070280.
[39] Chatel G. How sonochemistry contributes to green chemistry? Ultrason Sonochem 2018;40:117–22. https://doi.org/10.1016/j.ultsonch.2017.03.029.
[40] Fuentes-García JA, Carvalho Alavarse A, Moreno Maldonado AC, Toro-Córdova A, Ibarra MR, Goya GF. Simple sonochemical method to optimize the heating efficiency of magnetic nanoparticles for magnetic fluid hyperthermia. ACS Omega 2020;5:26357–64. https://doi.org/10.1021/acsomega.0c02212.
[41] Ravelo-Acuña D, Fuentes-García JA, Yee-Madeira HT, Diaz-Cano AI, Goya GF, Santoyo-Salazar J. Sonochemical magnetite encapsulation in silica at low irradiation power. Mater Lett 2019;250(1):103–7. https://doi.org/10.1016/j.matlet.2019.04.073.
[42] Ikram S, Ashraf F, Alzaid M, Mahmood K, Amin N, Haider SA. Role of nature of rare earth ion dopants on structural, spectral, and magnetic properties in spinel ferrites. J Supercond Nov Magn 2020:1–7. https://doi.org/10.1007/S10948-020-05723-8. 2020.
[43] Lai JY, Twaiq F, Ngu LH. Recycling of surfactant template in mesoporous MCM-41 synthesis. IOP Conf Ser Mater Sci Eng 2017;206:012044. https://doi.org/10.1088/1757-899X/206/1/012044.
[44] Li SW, Yang Z, Gao RM, Zhang G, Zhao J she. Direct synthesis of mesoporous SRL-POM@MOF-199@MCM-41 and its highly catalytic performance for the oxidesulfurization of DBT. Appl Catal B Environ 2018;221:574–83. https://doi.org/10.1016/j.apcatb.2017.09.044.
[45] Feng J, Wang Z, Shen B, Zhang L, Yang X, He N. Effects of template removal on both morphology of mesoporous silica-coated gold nanorod and its biomedical application. RSC Adv 2014;4(54):28683–90. https://doi.org/10.1039/c4ra03122a.
[46] Wang X, Zhang Y, Luo W, Elzatahry AA, Cheng X, Alghamdi A, et al. Synthesis of ordered mesoporous silica with tunable morphologies and pore sizes via a nonpolar solvent-assisted stöber method. Chem Mater 2016;28(7):2356–62. https://doi.org/10.1021/acs.chemmater.6b00499.
[47] Gao F, Lu Q, Liu X, Yan Y, Zhao D. Controlled synthesis of semiconductor PbS nanocrystals and nanowires inside mesoporous silica SBA-15 phase. Nano Lett 2001;1(12):743–8. https://doi.org/10.1021/nl0156383.
[48] Jin D, Lee JH, Seo ML, Jaworski J, Jung JH. Controlled drug delivery from mesoporous silica using a pH-response release system. New J Chem 2012;36:1616–20. https://doi.org/10.1039/C2NJ20976D.
[49] Luo L, Liang Y, Erichsen ES, Anwander R. Hierarchical mesoporous organosilica–silica core–shell nanoparticles capable of controlled fungicide release. Chem-A Eur J 2018;24(28):7200–9. https://doi.org/10.1002/chem.201800135.
[50] Guillet-Nicolas R, Bérubé F, Thommes M, Janicke MT, Kleitz F. Selectively tuned pore condensation and hysteresis behavior in mesoporous SBA-15 silica: correlating material synthesis to advanced gas adsorption analysis. J Phys Chem C 2017;121(44):24505–26. https://doi.org/10.1021/acs.jpcc.7b06745.
[51] Wang Y, Sun Y, Wang J, Yang Y, Li Y, Yuan Y, et al. Charge-reversal APTES-modified mesoporous silica nanoparticles with high drug loading and release controllability. ACS Appl Mater Interfaces 2016;8(27):17166–75. https://doi.org/10.1021/acsami.6b05370.
[52] Gibson AM, Bratchell N, Roberts TA. The effect of sodium chloride and temperature on the rate and extent of growth of

Clostridium botulinum type A in pasteurized pork slurry. J Appl Bacteriol 1987;62:479–90. https://doi.org/10.1111/j.1365-2672.1987.tb02680.x.
[53] Tjørve KMC, Tjørve E. The use of Gompertz models in growth analyses, and new Gompertz-model approach: an addition to the Unified-Richards family. PLoS One 2017;12:e0178691. https://doi.org/10.1371/journal.pone.0178691.
[54] Costa P, Sousa Lobo JM. Modeling and comparison of dissolution profiles. Eur J Pharm Sci 2001;13:123–33. https://doi.org/10.1016/S0928-0987(01)00095-1.
[55] Kowalczyk D, Pytka M, Szymanowska U, Skrzypek T, Łupina K, Biendl M. Release kinetics and antibacterial activity of potassium salts of iso-α-acids loaded into the films based on gelatin, carboxymethyl cellulose and their blends. Food Hydrocoll 2020;109:106104. https://doi.org/10.1016/J.FOODHYD.2020.106104.
[56] Esperanza Adrover M, Pedernera M, Bonne M, Lebeau B, Bucalá V, Gallo L. Synthesis and characterization of mesoporous SBA-15 and SBA-16 as carriers to improve albendazole dissolution rate. Saudi Pharm J 2020;28:15–24. https://doi.org/10.1016/J.JSPS.2019.11.002.
[57] Ritter A, Muñoz-Carpena R. Performance evaluation of hydrological models: statistical significance for reducing subjectivity in goodness-of-fit assessments. J Hydrol 2013;480:33–45. https://doi.org/10.1016/J.JHYDROL.2012.12.004.
[58] Torres TE, Lima E, Mayoral A, Ibarra A, Marquina C, Ibarra MR, et al. Validity of the Néel-Arrhenius model for highly anisotropic CoxFe3-xO4 nanoparticles. J Appl Phys 2015;118:183902. https://doi.org/10.1063/1.4935146.
[59] ASTM F 756-00. Standard practice for assessment of hemolytic properties of materials. Annu. B. ASTM Stand. 2008.
[60] Zhang Y, Yue Q, Zagho MM, Zhang J, Elzatahry AA, Jiang Y, et al. Core-shell magnetic mesoporous silica microspheres with large mesopores for enzyme immobilization in biocatalysis. ACS Appl Mater Interfaces 2019;11:10356–63. https://doi.org/10.1021/acsami.8b18721.
[61] Asgari M, Soleymani M, Miri T, Barati A. A robust method for fabrication of monodisperse magnetic mesoporous silica nanoparticles with core-shell structure as anticancer drug carriers. J Mol Liq 2019;292:111367. https://doi.org/10.1016/j.molliq.2019.111367.
[62] Peralta ME, Jadhav SA, Magnacca G, Scalarone D, Mártire DO, Parolo ME, et al. Synthesis and in vitro testing of thermoresponsive polymer-grafted core-shell magnetic mesoporous silica nanoparticles for efficient controlled and targeted drug delivery. J Colloid Interface Sci 2019;554(15):198–205. https://doi.org/10.1016/j.jcis.2019.02.086.
[63] Knežević NZ, Ruiz-Hernández E, Hennink WE, Vallet-Regí M. Magnetic mesoporous silica-based core/shell nanoparticles for biomedical applications. RSC Adv 2013;3:9584–93. https://doi.org/10.1039/c3ra23127e.
[64] Krupička S, Novák P. Oxide spinels. Handb Ferromagn Mater 1982;3:189–304. https://doi.org/10.1016/S1574-9304(05)80090-2.
[65] Vamvakidis K, Katsikini M, Sakellari D, Paloura EC, Kalogirou O, Dendrinou-Samara C. Reducing the inversion degree of $MnFe_2O_4$ nanoparticles through synthesis to enhance magnetization: evaluation of their 1H NMR relaxation and heating efficiency. Dalt Trans 2014;43:12754–65. https://doi.org/10.1039/c4dt00162a.
[66] Sanz B, Cabreira-Gomes R, Torres TE, Valdés DP, Lima E, De Biasi E, et al. Low-dimensional assemblies of magnetic $MnFe_2O_4$ nanoparticles and direct in vitro measurements of enhanced heating driven by dipolar interactions: implications for magnetic hyperthermia. ACS Appl Nano Mater 2020;3:8719–31. https://doi.org/10.1021/acsanm.0c01545.
[67] Keshavarz Hasan, Khavandi Alireza, Alamolhoda Somaye, Reza Naimi-Jamal M. pH-Sensitive magnetite mesoporous silica nanocomposites for controlled drug delivery and hyperthermia. RSC Adv 2020;10:39008–16. https://doi.org/10.1039/D0RA06916G.
[68] Mary Jacintha A, Umapathy V, Neeraja P, Rex Jeya Rajkumar S. Synthesis and comparative studies of $MnFe_2O_4$ nanoparticles with different natural polymers by sol–gel method: structural, morphological, optical, magnetic, catalytic and biological activities. J Nanostr Chem 2017;7:375–87. https://doi.org/10.1007/s40097-017-0248-z.
[69] Alahmadi SM, Mohamad S, Maah MJ. Synthesis and characterization of mesoporous silica functionalized with Calix[4]arene derivatives. Int J Mol Sci 2012;13:13726–36. https://doi.org/10.3390/ijms131013726.
[70] Sahoo S, Chakraborti CK, Behera PK, Mishra SC. FTIR and Raman spectroscopic investigations of a norfloxacin/carbopol934 polymeric suspension. J Young Pharm 2012;4:138–45. https://doi.org/10.4103/0975-1483.100017.
[71] Bhattacharyya S, Han R, Joshi JN, Zhu G, Lively RP, Walton KS, et al. Stability of zeolitic imidazolate frameworks in $NO_2$. J Phys Chem C 2019;123:2336–46. https://doi.org/10.1021/acs.jpcc.8b11377.
[72] Nyquist R. Alcohols and phenols. Interpret. infrared, Raman, nucl magn reson spectra. Elsevier; 2001. p. 125–41. https://doi.org/10.1016/b978-012523475-7/50171-6.
[73] Paul G, Musso GE, Bottinelli E, Cossi M, Marchese L, Berlier G. Investigating the interaction of water vapour with aminopropyl groups on the surface of mesoporous silica nanoparticles. Chem Phys Chem 2017;18:839–49. https://doi.org/10.1002/cphc.201601135.
[74] Okoye-Chine CG, Mbuya COL, Ntelane TS, Moyo M, Hildebrandt D. The effect of silanol groups on the metal-support interactions in silica-supported cobalt Fischer–Tropsch catalysts. a temperature programmed surface reaction. J Catal 2020;381:121–9. https://doi.org/10.1016/j.jcat.2019.10.036.
[75] Maleki A, Taheri-Ledari R, Rahimi J, Soroushnejad M, Hajizadeh Z. Facile peptide bond formation: effective interplay between isothiazolone rings and silanol groups at silver/iron oxide nanocomposite surfaces. ACS Omega 2019;4:10629–39. https://doi.org/10.1021/acsomega.9b00986.
[76] Sing KSW. Reporting physisorption data for gas/solid systems. Pure Appl Chem 1982;54:2201–18. https://doi.org/10.1351/pac198254112201.
[77] Rouquerol J, Rouquerol F, Llewellyn P, Maurin G. Adsorption by powders and porous solids: principles, methodology and applications. 2013.
[78] Schiith F, Sing W, Weitkamp J. Handbook of porous solids. Wiley; 2002. https://doi.org/10.1002/9783527618286.
[79] Adam A, Parkhomenko K, Duenas-Ramirez P, Nadal C, Cotin G, Zorn P-E, et al. Orienting the pore morphology of core-shell magnetic mesoporous silica with the sol-gel temperature. Influence on MRI and magnetic hyperthermia properties. Molecules 2021;26:971. https://doi.org/10.3390/molecules26040971.
[80] Narayan R, Nayak UY, Raichur AM, Garg S. Mesoporous silica nanoparticles: a comprehensive review on synthesis and recent advances. Pharmaceutics 2018;10(118). https://doi.org/10.3390/pharmaceutics10030118.
[81] Farhadian N. How doxorubicin anticancer drug interacts with folic acid and APTES functional groups: a first principle study. J Nanomed Res 2014;6. https://doi.org/10.15406/JNMR.2017.06.00150.
[82] Peppas NA, Narasimhan B. Mathematical models in drug delivery: how modeling has shaped the way we design new

drug delivery systems. J Contr Release 2014;190:75–81. https://doi.org/10.1016/j.jconrel.2014.06.041.

[83] Di Crescenzo A, Spina S. Analysis of a growth model inspired by Gompertz and Korf laws, and an analogous birth-death process. Math Biosci 2016;282:121–34. https://doi.org/10.1016/j.mbs.2016.10.005.

[84] Baishya H. Application of mathematical models in drug release kinetics of carbidopa and levodopa ER tablets. J Dev Drugs 2017;6:1–8. https://doi.org/10.4172/2329-6631.1000171.

[85] Tewes F, Munnier E, Antoon B, Ngaboni Okassa L, Cohen-Jonathan S, Marchais H, et al. Comparative study of doxorubicin-loaded poly(lactide-co-glycolide) nanoparticles prepared by single and double emulsion methods. Eur J Pharm Biopharm 2007;66:488–92. https://doi.org/10.1016/J.EJPB.2007.02.016.

[86] Wadhwa R, Aggarwal T, Thapliyal N, Kumar A, Priya Yadav P, Kumari V, et al. Red blood cells as an efficient in vitro model for evaluating the efficacy of metallic nanoparticles. 3 Biotech 2019;9:279. https://doi.org/10.1007/s13205-019-1807-4.

[87] Wang S, Konorev EA, Kotamraju S, Joseph J, Kalivendi S, Kalyanaraman B. Doxorubicin induces apoptosis in normal and tumor cells via distinctly different mechanisms: intermediacy of $H_2O_2$- and p53-dependent pathways. J Biol Chem 2004;279:25535–43. https://doi.org/10.1074/jbc.M400944200.

[88] Foglia S, Ledda M, Fioretti D, Iucci G, Papi M, Capellini G, et al. In vitro biocompatibility study of sub-5 nm silica-coated magnetic iron oxide fluorescent nanoparticles for potential biomedical application. Sci Rep 2017;7:46513. https://doi.org/10.1038/srep46513.

[89] McConnell KI, Shamsudeen S, Meraz IM, Mahadevan TS, Ziemys A, Rees P, et al. Reduced cationic nanoparticle cytotoxicity based on serum masking of surface potential. J Biomed Nanotechnol 2016;12(1):154–64. https://doi.org/10.1166/jbn.2016.2134.